



Long-term vertical-land-motion investigation with space and terrestrial geodetic techniques near San Leon, Texas, USA

Xiaojun Qiao^{a,b}, Tianxing Chu^{a,b,*}, Philippe Tissot^{b,c}, Seneca Holland^b

^a Department of Computer Science, Texas A&M University-Corpus Christi, 6300 Ocean Drive, Corpus Christi, TX 78412, USA

^b Conrad Blucher Institute for Surveying and Science, Texas A&M University-Corpus Christi, 6300 Ocean Drive, Corpus Christi, TX 78412, USA

^c Department of Physical and Environmental Sciences, Texas A&M University-Corpus Christi, 6300 Ocean Drive, Corpus Christi, TX 78412, USA

ARTICLE INFO

Keywords:

InSAR
GNSS
Sea-level observations
Coastal subsidence
Long-term time series

ABSTRACT

Monitoring vertical land motion (VLM) along coastlines, which influences the dynamics of sea level changes in relation to the land, is a challenging task due to its inherent high spatiotemporal variability and limited availability of observations. This study aimed to investigate the rates, patterns, and drivers of land subsidence near the coastal town of San Leon, TX, United States, since the 1990s, utilizing a range of space and terrestrial geodetic techniques. These techniques included interferometric synthetic aperture radar (InSAR), global navigation satellite systems (GNSS), tide gauge (TG), and satellite radar altimetry (SRA). The small baseline subset (SBAS) InSAR method was adopted to process 254 images from three synthetic aperture radar (SAR) sensors, i.e., ERS-2 between 1995 and 1999, ALOS-1 PALSAR between 2006 and 2011, and Sentinel-1 between 2016 and 2020. The results from InSAR subsidence maps were verified by comparing with high-accuracy vertical positioning observations at ten continuously operating GNSS (cGNSS) stations. Within the study area, a special attention was given to the Eagle Point TG station where sea level has been significantly rising relative to the sinking land. Long-term time series of land subsidence at Eagle Point obtained from sea-level difference between TG and SRA observations were confirmed and compared against InSAR and the cGNSS station observations recorded in close proximity. Gaussian Process regression (GPR) was then employed to model the VLM processes at Eagle Point using: (1) the combined results of InSAR and sea-level difference (i.e., GPR 1), and (2) the InSAR results alone (i.e., GPR 2). A 0.9 mm/yr divergence was found between GPR 1 and GPR 2 models, indicating the potential to accurately estimate long-term VLM with InSAR standalone measurements even if multi-year observation gaps intermittently occur, especially for inland areas where measurement data from other geodetic techniques, such as GNSS, TG, and SRA, are not available. Further investigations suggest that land subsidence around Eagle Point since 1998 was related to anthropogenic activities such as hydrocarbon pumping from oil and gas wells that were situated in close proximity to the TG station.

1. Introduction

Land subsidence is the gradual or sudden downward motion of Earth's surface as a result of natural processes (e.g., glacial isostatic adjustment, compaction and sedimentation, and tectonic movements) and/or anthropogenic activities (e.g., extraction of water, oil, and gas) (Shirzaei et al., 2021). Land subsidence, a worldwide challenge, causes a wide spectrum of environmental, geological and economic problems such as regional tilting, ground ruptures, damages to infrastructures, and increased risk of flooding (Holzer and Johnson, 1985). It was reported that more than 44,000 square km of land across 45 states in the U.S. has been directly affected by land subsidence, resulting in

over \$125 million of annual economic losses (Galloway et al., 1999; National Research Council, 1991).

Consequences of land subsidence may be exacerbated in low-lying coastal areas, home to ten percent of global population, where sea water may move inland in wake of rising sea levels relative to subsiding lands (McGranahan et al., 2007). A prior study revealed that the rate of local land subsidence could be tenfold or more compared with that of global mean sea-level rise (Woodworth et al., 2019). For example, in some major coastal cities, the peak velocity of land subsidence ranged between −16 and −43 mm/yr (Tay et al., 2022). Meanwhile, the estimated global sea level rose by around 3 mm/yr observed by satellite altimeters (Chen et al., 2017). Accurate estimation of the magnitude

* Corresponding author at: Department of Computer Science, Texas A&M University-Corpus Christi, 6300 Ocean Drive, Corpus Christi, TX 78412, USA.

E-mail address: tianxing.chu@tamucc.edu (T. Chu).

<https://doi.org/10.1016/j.jag.2023.103580>

Received 31 May 2023; Received in revised form 2 November 2023; Accepted 18 November 2023

Available online 22 November 2023

1569-8432/© 2023 The Author(s). Published by Elsevier B.V. This is an open access article under the CC BY license (<http://creativecommons.org/licenses/by/4.0/>).

and rate of coastal subsidence is, therefore, considered a key element in discovering and modeling the patterns of local land–water interactions to facilitate data-informed decision making for stakeholders such as conservation managers, urban planners, and emergency response personnel.

With the advent of the global navigation satellite systems (GNSS), high-precision positioning results can be obtained through static and continuous observations of code and phase measurements from a geodetic-grade dual-frequency receiver at the millimeter level (Wang and Soler, 2015). Over the past two decades, a large number of continuously operating GNSS (cGNSS) stations have been installed to support scientific needs worldwide (Blewitt et al., 2018). During this time, the investigation of accurate land motion and sea-level change with positioning data collected by cGNSS stations has gained traction. For example, positioning results obtained from cGNSS stations were applied to combine with water-level data received at near-located tide gauge (TG) stations for an estimation of consistent sea-surface trends (Wöppelmann et al., 2007). However, creating an accurate and large-scale coastal land subsidence map using only observations from the cGNSS network is challenging. This is because: (1) the considerable variation in land deformation velocity across different locations makes it essential to deploy a substantial number of cGNSS stations to effectively capture the diverse spatial patterns (Tang et al., 2021); (2) only a small number of cGNSS stations were installed near a coastline with an extended observation history of 15 years or more (Yu and Wang, 2017); and (3) long-term cGNSS observations are subject to interruptions in wake of natural and anthropogenic events such as hardware failure or upgrade, power outage, and natural disasters (Zilkoski et al., 2003; Crocetti et al., 2021; Blewitt et al., 2018).

Growing attention has been paid to monitoring vertical land motion (VLM), including instances of both land subsidence and uplift along the coastlines with the synthetic aperture radar (SAR) interferometry technique. Interferometric SAR (InSAR) can provide high-accuracy VLM results to an extensive imaged geographical area (Simons and Rosen, 2007). The InSAR results display in the form of relative displacement time series, both spatially and temporally, requiring external data sources (Castellazzi et al., 2021; Chen et al., 2021), such as GNSS to transform the results referenced to a geodetic datum. For instance, multi-platform SAR sensors acquire radar images of the same area from different looking angles and at different times, and their InSAR VLM time series need to properly align with long-term stable GNSS positioning results (Qu et al., 2015; Chen et al., 2021). However, challenges arise in constructing long-term coastal subsidence results with InSAR and GNSS data due to limited number of cGNSS stations along the coastlines with sufficient availability (e.g., 20 years or more).

On the other hand, sea-level data obtained from TGs and satellite radar altimeters (SRAs) emerged as promising observations for the purpose of estimating coastal subsidence (Cazenave et al., 1999; Qiao et al., 2021). One advantage of using sea-level measurements for subsidence analysis is the relatively long temporal observation overlaps between TG and SRA data, which can reach up to 30 years depending on the locations. However, VLM results obtained from sea-level observations are susceptible to the influence of sea-level variations, specifically the inter-annual to decadal variability inherent in time series (Woodworth et al., 2019). As a result, previous studies using sea-level observations have predominantly focused on long-term trends alone, rather than considering VLM from a time-series perspective (Kuo et al., 2004; Santamaría-Gómez et al., 2014; Letetrel et al., 2015; Wöppelmann and Marcos, 2016). Constructing reliable VLM time series using sea-level observations is a challenging yet important task for understanding land motion processes, particularly in close proximity to TG stations and gaining insights into water–land interactions. Previous studies have demonstrated the feasibility of constructing VLM time series by comparing trend values with GNSS observations in the Texas Coast region (Qiao et al., 2022, 2023a). Nevertheless, validating and

comprehending VLM time-series results derived from sea-level observations may necessitate additional efforts in acquiring multiple sources of information.

Given the aforementioned practical complexities associated with monitoring VLM, the utilization of results obtained from various sources is expected to increase the likelihood of revealing, validating, and comprehending coastal subsidence (Wang et al., 2022). This study focuses on the integration of multiple space and terrestrial geodetic techniques including InSAR, GNSS, SRA and TG to investigate long-term coastal subsidence since the 1990s near the coastal town of San Leon, TX, with a focus on the Eagle Point TG station. The specific objectives are to:

- (1) Obtain the VLM estimates from multiple spaceborne synthetic aperture radar (SAR) platforms between 1995 and 2020 with InSAR and GNSS data near the coastal town of San Leon, TX;
- (2) Evaluate the performance of VLM rates estimated with the sea-level difference method using TG and SRA observations (Qiao et al., 2022) by comparing against the displacement time series obtained from InSAR and GNSS in the immediate vicinity of the Eagle Point TG station; and
- (3) Identify the potential causes behinds observed coastal subsidence at the Eagle Point TG station.

2. Study area and data

2.1. Study area

The study area covers 1392 km², corresponding to a bounding box from 29.33°N to 29.68°N and from 95.25°W to 94.88°W, as indicated by the blue rectangle in Fig. 1. The study area was selected in a consideration of: (1) including the continuously operating Eagle Point TG station 8771013 (NOAA, 2023a) within the city limit of San Leon, TX, USA, and (2) the fact that the sea-level rise trend measured at Eagle Point TG station has reached 12.5 mm/yr between 1992 and 2012, which was almost twice as great as the trends of its nearby TG stations (Epps and Khan, 2016; Zhong et al., 2022). Eagle Point is also the epicenter of high tide flooding (HTF), occurring when the sea level is over half a meter above high tide measured by National Oceanic and Atmospheric Administration (NOAA)'s TGs. The HTF frequency reached 38 days in 2020 (Sweet et al., 2021). Geologically speaking, the Chicot and Evangeline aquifers are the main groundwater sources in the Texas Gulf Coast aquifer system (Galloway et al., 1999). Activities related to groundwater withdrawal, oil/gas extraction, and sinkhole collapse at salt domes are thought to be potential drivers behind the observed and reported land subsidence near this area (Qu et al., 2015; Galloway et al., 1999).

Across the entire Texas Gulf Coast, both transgressive marine sediments and regressive marine/non-marine sediments were deposited during the Tertiary period, resulting in a primary lithology of interbedded sand and shale (Gregory, 1966; Galloway et al., 1982). An overall stratigraphic illustration of related formations over the Texas Gulf can be found in Table S1 of the supplementary file, and the formation records of a gas well near the Eagle Point TG, provided by the Railroad Commission (RRC) of Texas (RRC, 2023), are shown in Table S2 of the supplementary file. Regarding oil/gas exploration, there are three main formations including: the Vicksburg formation of early Oligocene, the Frio formation of middle Oligocene, and the Anahuac of late Oligocene (Gregory, 1966). In both Frio and Vicksburg formations, fluvial and deltaic environments as well as associated processes facilitated two depocenters separated by the San Marcos arch: the Houston Embayment of Southeast Texas and the Rio Grande Embayment of the South Texas Gulf (Galloway et al., 1982; Gregory, 1966; Combes, 1993). Both depositional processes and syn-depositional faults during deltas being constructed facilitated porous sands, which is believed to be favorable for generating hydrocarbon (Gregory, 1966; Hyne, 1984). Besides, the Houston Embayment is characterized by salt diapirs (Galloway et al., 1982; Combes, 1993).

Table 1
SAR data acquisitions and corresponding sensor information used in this study.

Direction	ERS-2	ALOS-1 PALSAR	Sentinel-1	
	Descending	Ascending	Ascending	Descending
Path	212	175	34	143
Frame	3015	570, 580	90	492
Polarization	VV	HH	VV	VV
Wavelength	5.6 cm	23.6 cm	5.5 cm	5.5 cm
Revisit period	35 days	46 days	12 days	12 days
Image number	18	10 (each frame)	102	113
Temporal range	Dec. 1995–Jul. 1999	Dec. 2006–Jan. 2011	Sep. 2016–Jun. 2020	Oct. 2016–Jun. 2020

2.2. Data

2.2.1. SAR

A total of 243 SAR images corresponding to three spaceborne SAR platforms (i.e., ERS-2, ALOS-1 PALSAR, and Sentinel-1) were utilized to form long-term displacement time series between 1995 and 2020. It should be noted that SAR images captured by the ALOS-1 PALSAR in the two frames were merged and processed collectively. For the particular study area, time frame, and SAR missions employed, only Sentinel-1 SAR images were available in both ascending and descending orbits. A total of four SAR collections were used in this study, namely ERS-2 descending, ALOS-1 PALSAR ascending, Sentinel-1 ascending, and Sentinel-1 descending. The spatial coverage of SAR images is shown in Fig. 1 with sensor names and path/frame numbers marked at the top or bottom of the corresponding box. The ERS-2 data were accessed through UNAVCO (UNAVCO, 2022), and ALOS-1 PALSAR (i.e., L1.0 data) and Sentinel-1 SAR collections were obtained from the Alaska Satellite Facility (ASF) (ASF, 2022). Detailed information on the SAR data collections as well as the corresponding sensor characteristics can be found in Table 1. SAR image acquisition dates corresponding to four SAR datasets can be found in Table S3 to S6 in the supplementary file. Precise orbit data, provided by the Delft Institute for Earth-Oriented Space Research (DEOS), were used to facilitate the processing of the ERS-2 data (Scharroo and Visser, 1998; DEOS, 2022). For removing the topographic phase component contained in the interferograms, the 1 arcsec, or approximately 30-m, resolution Shuttle Radar Topography Mission (SRTM) digital elevation model (DEM) (Earth Resources Observation and Science (EROS) Center, 2017) was used in ISCE (Rosen et al., 2012). Copernicus DEM GLO-30 was adopted by ASF's Hybrid Pluggable Processing Pipeline (HYP3), a cloud-based system that provides on-demand Sentinel-1 InSAR processing using the GAMMA software (Hogenson et al., 2016).

2.2.2. GNSS

Positioning data obtained from a total of 11 cGNSS stations were included for result validation and analysis purposes (Fig. 1), spanning between 1995 and 2020 depending on data availability. These cGNSS stations belong to multiple cGNSS networks, including five stations (i.e., COTM, MEPP, NASA, UHCO, and UHCL) from HoustonNet operated and maintained by the University of Houston, two (i.e., P036 and PA00) from the PAM network run by the Harris-Galveston Subsidence District (HGSD), two (i.e., TXAV and TXLQ) from SmartNet North America (Hexagon, 2023), one (i.e., TXLM) from the Texas Department of Transportation (TxDOT), and one (i.e., DEN4) from UNAVCO (Yu and Wang, 2017; Zilkoski et al., 2003). Most cGNSS antennas were attached to buildings or mounted on poles inserted securely below the soil. DEN4 is the only cGNSS station at which the antenna was mounted on a wellhead. Specific details of these cGNSS stations can be found in Table S7. PAM stations collected GNSS data on a per week basis because of scheduled routine rotation of surveying equipment among different sites (Zilkoski et al., 2003). The P036 station within the PAM network, located near Eagle Point, was included in this research for analyzing VLM results near the TG (Fig. 1). Raw GNSS observation data at P036 were accessed from HGSD and processed through NOAA's Online

Positioning User Service (OPUS) (NOAA, 2023c). Daily precise point positioning (PPP) solutions from the remaining ten cGNSS stations were directly accessed from the Nevada Geodetic Laboratory (NGL) (NGL, 2023), and were used mainly for validating InSAR results.

2.2.3. Sea-level data

Sea-level observations with six-minute or one-hour intervals between January 1, 1993, and March 8, 2020, were used to estimate VLM time series at the Eagle Point TG station (i.e., 8771 013). For a reliable estimate, three additional TG stations (i.e., 8771 450, 8770 570, and 8774 770) that possessed an observation history over 25 years between 1993 and 2020 were also employed. Sea level observations of these three TG stations maintained high correlations with that of the Eagle Point TG station. Correlation refers to the correlation coefficient calculated with the entire water-level time series between the Eagle Point TG station and each of those three supporting TG stations. Detailed information regarding those TG stations can be found in Table S8 in the supplementary file. Daily water levels were averaged from the raw data, and the mean value of the sea-level records between 1993 and 2020 was removed on a per station basis to ensure data consistency across different TG stations. The level-4 sea-surface height (SSH) product, interpolated as quarter-degree grid cells extracted from the initial SRA observations, was accessed from the Copernicus Marine Environment Monitoring Service (CMEMS) and was used to obtain the absolute sea-level change (ASLC) results (E.U. Copernicus Marine Service Information, 2022). Dynamic atmospheric corrections (DAC) data were applied to compensate water-level variations related to atmospheric winds and pressure contained in the daily SSH time series (LEGOS/CNRS/CLS, 1992). For each TG involved, the SSH data from the grid cell in closest proximity was utilized to derive the ASLC variable. The locations of SSH grid cells can be found in Table S8 of the supplementary file. Likewise, the time series of DAC were extracted from the nearest grid cell for each TG.

3. Methods

3.1. Overview

The study integrated space and terrestrial geodetic measurements obtained small baseline subset (SBAS), GNSS, SRA and TG observations to investigate long-term coastal subsidence since 1990s near San Leon, TX, and model the VLM pattern at the Eagle Point TG station. Additionally, this work also examined the connection between potential causes that resulting in subsidence at the area of interest and documented anthropogenic activities. The research workflow was summarized in Fig. 2. SBAS InSAR processing, as elaborated in Section 3.2, consists on interferogram generation and post-processing in the Miami InSAR Time-series software in PYTHON (MintPy) suite to produce land deformation time series and velocity estimates (Yunjun et al., 2019), which corresponds to the first two columns in Fig. 2. Four stacks of interferograms were generated and post-processed independently for SAR acquisitions of ERS-2, ALOS-1 PALSAR, Sentinel-1 ascending, and Sentinel-1 descending. Interferograms were generated from the InSAR Scientific Computing Environment (ISCE) software (Rosen et al., 2012) for ERS-2 and ALOS-1 SAR images, and from HYP3 for both Sentinel-1

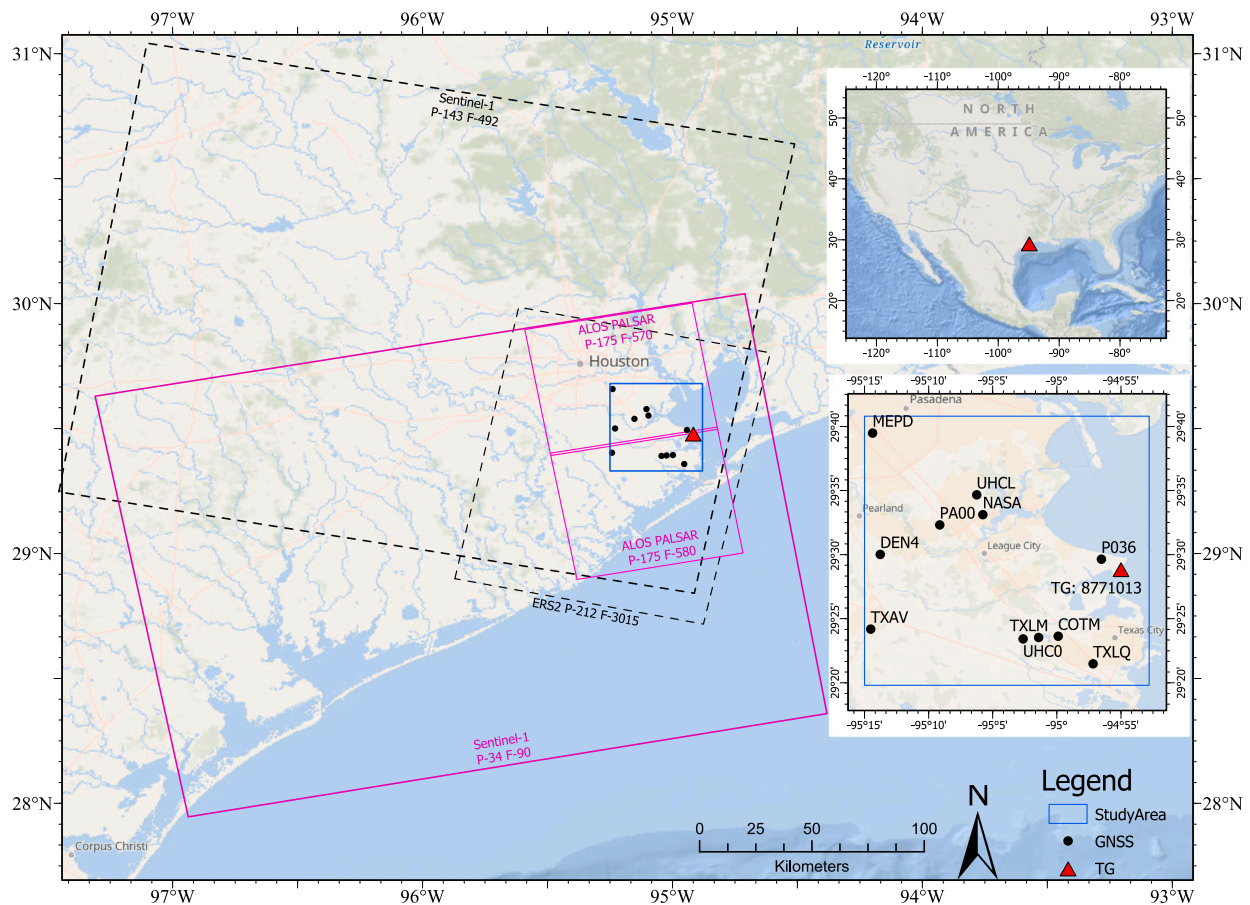


Fig. 1. Study area shown in the blue rectangle. Red triangle marks the location of the Eagle Point TG station (ID: 8771013) within the city limit of San Leon, TX. Black dashed boxes and pink solid boxes correspond to data coverage of the descending and ascending SAR acquisitions, respectively. Sensor name and path/frame numbers are marked at the top/bottom margin of a specific acquisition box. Both inset and reference maps are provided as guides on the right side of the figure. (For interpretation of the references to color in this figure legend, the reader is referred to the web version of this article.)

ascending and descending SAR data. InSAR displacement time series or velocity in the line-of-sight (LOS) direction were converted to the vertical direction using Sentinel-1's ascending and/or descending LOS results. Precise Point positioning (PPP) solutions of the 11 cGNSS stations were accessed from NGL or processed by OPUS on demand. Meanwhile, coastal subsidence was estimated using the sea-level difference between TG and SRA observations, as detailed in Section 3.5, at the Eagle Point TG station (i.e., 8771013). Finally, coastal subsidence time series from multiple space geodetic techniques were integrated for validation, quantification, and analysis of the subsidence processes over the study area.

3.2. InSAR processing

To qualify ground surface deformation, two main categories of InSAR techniques of multi-temporal InSAR (MT-InSAR) processing techniques have been developed: persistent scatterers (PS) and distributed scatterers (DS) (Yunjun et al., 2019). The PS method only focuses on phase-stable scatterers by comparing them with a single selected reference image (Hooper et al., 2004). SBAS, a typical DS InSAR method, aims to handle decorrelation and improving spatial coverage of available pixels by exploiting small spatial-temporal baseline connections (Yunjun et al., 2019; Berardino et al., 2002). To mitigate the impacts induced by infrequent acquisitions as well as their large spatial baselines obtained from SAR platforms that were decommissioned (i.e., ERS-2 and ALOS-1 PALSAR), the SBAS method was adopted in this research. Detailed parameter settings during InSAR processing can be found in

Table 2. The practical grid sizes were approximately 120 m for ERS-2, 90 m for ALOS-1 PALSAR, and 80 m for Sentinel-1 interferograms, respectively. The same sizes remained for subsequent outputs of the processing chain.

All stacks of interferograms were then independently passed to MintPy for estimating the LOS displacement time series. In each stack processing, network modification was conducted to exclude interferograms when the average coherence fell below specific thresholds by keeping a minimum spanning tree (MST). A reference point was chosen within the study area, which exhibited high coherence without obvious trend of land subsidence. Pixels of stacked SAR interferograms overlapping with water bodies were masked during MintPy processing. Differential phase delay due to the atmosphere was estimated by the Python based Atmospheric Phase Screen (PyAPS) module (Jolivet et al., 2011) using the ERA-5 data from European Centre for Medium-Range Weather Forecasts (ECMWF) (Hersbach and Dee, 2016). The LOS displacement time series were obtained after inverting the SBAS network of unwrapped interferograms and applying related corrections (Yunjun et al., 2019). Detailed key steps of MintPy processing can be found in Fig. 2.

3.3. Vertical deformation from LOS InSAR results

For Sentinel-1 data, reliable vertical land subsidence can be decomposed by combining the ascending and descending LOS results. Assuming a target SAR pixel is experiencing land deformation with the practical velocities of V_n , V_e , and V_u in the North, East, and Up

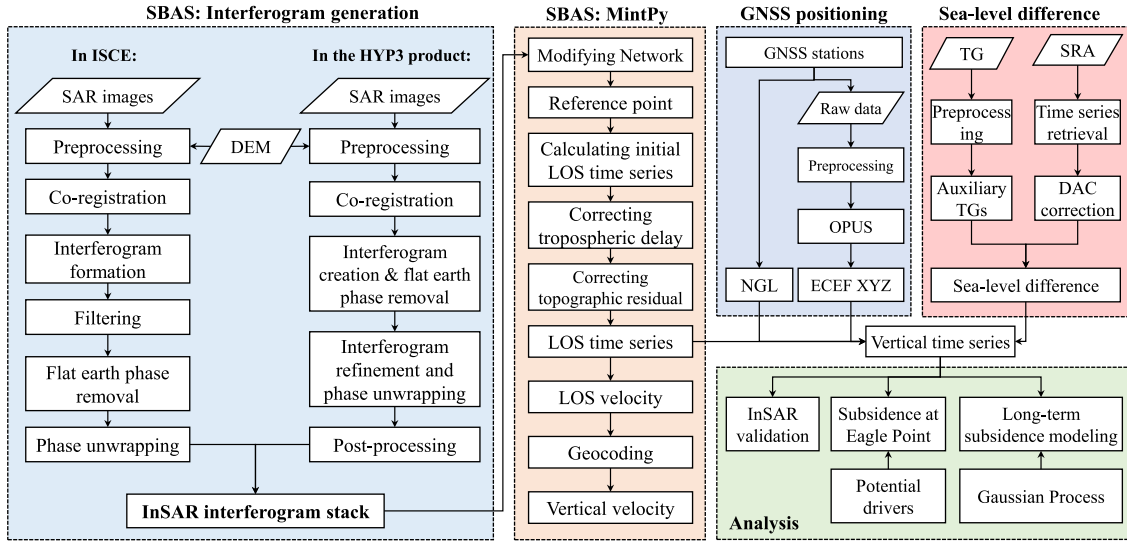


Fig. 2. Research workflow.

Table 2
InSAR processing parameters.

Parameters	ISCE	ALOS-1 PALSAR		HYP3
	ERS-2			Sentinel-1
Temporal baseline	< 700 days		< 700 days	< 60 days
Perpendicular baseline	< 1,000 m		< 2,500 m	< 200 m
Phase unwrapping	SNAPHU ^a		SNAPHU ^a	MCF ^b
Multi-looking number ^c	30 × 6		30 × 6	20 × 4

^a SNAPHU refers to statistical-cost network-flow algorithm for phase unwrapping (Chen and Zebker, 2002).

^b MCF is the minimum cost flow algorithm (Costantini, 1998; Hognson et al., 2016).

^c The multi-looking number is shown in azimuth × range measured in pixels.

directions respectively. Theoretically, the land deformation velocity V_{LOS} observed by InSAR in the LOS direction fulfills:

$$V_{LOS} = [V_n \sin \varphi - V_e \cos \varphi] \sin \theta + V_u \cos \theta \quad (1)$$

where φ is the satellite heading angle (positive clockwise from the north), θ is the radar incidence angle (Fialko et al., 2001). Because SAR satellites employed near-polar orbits, the LOS measurements are not sensitive to the north–south motion component of the ground displacement vector (Wright et al., 2004; Motagh et al., 2017), meaning that the north–south motion does not contribute significantly to the InSAR LOS displacement compared with the V_u and V_e components. By excluding the north component, unknowns of V_e and V_u can be then calculated with observations obtained from both ascending and descending orbits by solving Eq. (2):

$$\begin{bmatrix} -\cos \varphi^A \sin \theta^A & \cos \theta^A \\ -\cos \varphi^D \sin \theta^D & \cos \theta^D \end{bmatrix} \begin{bmatrix} V_e \\ V_u \end{bmatrix} = \begin{bmatrix} V_{LOS}^A \\ V_{LOS}^D \end{bmatrix} \quad (2)$$

where superscripts “A” and “D” correspond to the ascending and descending orbit observations, respectively. However, for ascending or descending only acquisitions (i.e., ERS-2 and ALOS-1 PALSAR in this study), Eq. (2) is not applicable, and the observation V_{LOS} was directly projected to the vertical direction in this study, by further assuming a zero East–West bound land motion as indicated by Eq. (3):

$$V_u = \frac{V_{LOS}}{\cos \theta} \quad (3)$$

In this study, Eqs. (2) and (3) were used to extract the vertical land motion velocity and to calculate vertical displacement time series from the LOS results.

3.4. GNSS

Online processing modules, for example the OPUS suite by NOAA (El Shouny and Miky, 2019), have been developed to allow users to achieve high accuracy GNSS positioning results without having to set up base stations for maintaining simultaneous observations. The OPUS tool computes survey-grade coordinates of a rover receiver using a double differenced and ionospheric-free mathematical model by averaging results from three independent single-baseline solutions within the continuously operating reference station (CORS) network (Soler et al., 2011).

The OPUS Static (OPUS-S) processes L1/L2 dual-frequency observations with a length of between two and 48 h and was adopted in the study to compute daily coordinates at the P036 cGNSS station for validating the VLM results near Eagle Point TG. Approximately 1 cm OPUS-S vertical accuracy was reported in processing 24-hour observations (Wang and Soler, 2013). Raw daily observation files at the P036 cGNSS station were accessed from HGSD, preprocessed and uploaded to OPUS repeatedly for PPP calculation. Resultant time-series of the Earth-centered, Earth-fixed (ECEF) coordinates in the 2014 ITRF reference frame were converted to the East-North-Up (ENU) directions relative to a local origin that is close to the P036 station with the pymap3d module (Hirsch, 2018).

The ECEF positioning time series for the remaining cGNSS stations (i.e., all cGNSS stations except P036) were provided by NGL (NGL, 2023), which adopts the GipsyX 1.0 suite (Bertiger et al., 2020) to process daily observation files across the globe and provides PPP solutions in the 2014 ITRF by utilizing precise GNSS orbit, clock data, and necessary corrections. The coordinates were then projected into the ENU directions the same way as was done for the P036 station.

3.5. VLM from sea-level difference

The difference between relative sea-level change (RSLC), measured by TG stations, and ASLC measured by SRAs, contains land deformation information (Qiao et al., 2021). To suppress high-frequency sea-level variations for a reliable coastal subsidence estimate, ASLC and RSLC variables were corrected with Eq. (4) before differencing operation (Qiao et al., 2022):

$$\begin{cases} ASLC(t) = A(t) - \frac{1}{q} \sum_{i=1}^q [A_{Q_i}(t) - f_{Q_i}(t)] \\ RSLC(t) = R(t) - D(t) - \frac{1}{q} \sum_{i=1}^q [R_{Q_i}(t) - D_{Q_i}(t) - g_{Q_i}(t)] \end{cases} \quad (4)$$

where $A(t)$, $R(t)$, and $D(t)$ correspond to SRA, TG, and DAC observation, respectively, at the Eagle Point TG station (i.e., 8771013). Square brackets in Eq. (4) were used to calculate the sea-level variability using a set of high-correlated TG stations, i.e., $Q = \{8770570, 8771450, 8774770\}$, as detailed in Table S8. The variable q is the number of stations in Q , and $f_{Q_i}(t)$ and $g_{Q_i}(t)$ are the linear regression models for $A_{Q_i}(t)$ and $R_{Q_i}(t)$ time series, respectively. Finally, coastal subsidence time series can be estimated with the sea-level difference of $ASLC(t) - RSLC(t)$. Detailed description of the method can be found in Qiao et al. (2022).

4. Results

4.1. InSAR time series and velocity estimation

The study adopted average spatial coherence thresholds of 0.35 for ERS-2, 0.60 for ALOS-1 PALSAR, 0.50 for Sentinel-1 ascending, and 0.60 for Sentinel-1 descending data to exclude some low-coherence interferograms. Such thresholds came as a consideration of practical coherence capabilities related to the SAR-sensor characteristics across different acquisitions, such as revisit frequency, radar signal wavelength, and so forth. Besides, considering the L-band ALOS-1 data tend to be easily affected by ionospheric delay (Zhu et al., 2019), some interferograms in ALOS-1 PALSAR were further excluded via manual inspection given that no ionospheric corrections were conducted in MintPy processing in this study. As a result, a total of 861 interferograms remained and were used for time series analysis, including 35 from ERS-2, 20 from ALOS-1 PALSAR, 388 from Sentinel-1 ascending, and 418 from Sentinel-1 descending acquisitions, as shown in Fig. 3. Each subplot in Fig. 3 shows the scatter plot between the perpendicular and temporal baselines, as well as the possible connection corresponding to an interferogram for each of the four SAR datasets.

Displacement time series were calculated on a per pixel basis for each of the SAR data collections from a redundant differential SBAS network as shown in Fig. 3. A land deformation trend was then estimated using time series at each pixel, and the LOS velocity map for each SAR collection is illustrated in Fig. 4, where deformation patterns are distinct across different SAR platforms, e.g., the South of the study area. Similar spatial patterns manifest between Sentinel-1 ascending and descending acquisitions as shown in Fig. 4(c) and (d), although they were based on two different LOS directions, implying that the land motion of the study area occurred mainly to the vertical dimension. Besides, the deformation rate over the same area may vary over time across different SAR platforms in their corresponding LOS directions. For example, the city of Seabrook, TX, as boxed in red in Fig. 4(a), demonstrated stronger LOS deformation in the late 1990s as imaged by the ERS-2 sensor. Vertical velocity was calculated as per Eq. (2) for Sentinel-1 by combining both ascending and descending results, as illustrated in Fig. 5. In order to maintain the clarity and conciseness of the presentation, the vertical velocity maps from the ERS-2 and ALOS-1 LOS results, computed as dictated by Eq. (3), are not showcased.

4.2. InSAR time-series validation

InSAR results derived from the four SAR data collections were validated through ten cGNSS stations. Specifically, displacement time series in the vertical direction of each cGNSS station were compared against that of the InSAR grid cell in the closest proximity, as shown in Fig. 6. ERS-2 and ALOS-1 PALSAR sensors actively illuminated the ground with average radar angles of inclination of 23.2° and 39.7°, respectively, and their vertical time series were converted from single orbit LOS results using Eq. (3). Ascending and descending results of Sentinel-1 were first averaged to the monthly mean and then decomposed into vertical as per Eq. (2) on a per month basis. In Fig. 6, time series of InSAR results were vertically shifted to be superimposed on GNSS results for better visual comparison. It is worth noting that this intentional vertical shift on InSAR results did not alter the nature of the main focus in the study on VLM rate estimate. Among the ten cGNSS stations (Fig. 5), there are two stations covering the time span of both ALOS-1 and Sentinel-1 sensors between 2007 and 2020, i.e., in Fig. 6(f) and (j), and only one station covering the whole period of the three SAR platforms between 1995 and 2020 (i.e., Fig. 6(j)).

In Fig. 6, overall good agreement can be observed from the time-series comparison between InSAR and GNSS in terms of the trend and variations. However, there is a notable divergence in the VLM trend obtained between InSAR and the DEN4 cGNSS station as shown in Fig. 6(b). This is likely because the DEN4 antenna was rigidly mounted on the wellhead (Fig. 7), and the well was drilled down through the subsurface. Therefore, its GNSS measurements may reflect the subsurface subsidence, while SBAS InSAR measured land-surface deformation of a specific multi-looked grid cell. In addition, visible divergence between InSAR and GNSS also appears at other locations (e.g., Fig. 6(g)). Possible reasons for potential divergences in the InSAR vs. GNSS comparison include: (1) the InSAR technique delivers an average land-deformation rate within a specific grid cell depending on the spatial resolution between 80 and 120 m in this study while GNSS measures VLM on particular point locations, (2) GNSS antennas at some stations were anchored below the land surface as indicated in Table S7 while InSAR reveals land surface deformation, and (3) InSAR results are affected by phase decorrelation related to baseline/geometry, terrain changes like vegetated area, and so forth (Hanssen, 2001).

4.3. OPUS GNSS positioning

Among all the cGNSS stations employed in the study, the results from the P036 station were used to compare with that obtained from InSAR and sea-level observations in the immediate vicinity of the Eagle Point TG station. The vertical displacement at P036 is shown as blue squares in Fig. 8. As mentioned in Section 2.2.2, a GNSS antenna was installed on a PAM station at a regular rotational interval to collect data, resulting in potential height abrupt variations due to antenna changes. Dates at the four visually obvious vertical shifts in Fig. 8 were assumed as steps related to antenna changes, resulting in five time series segments. To facilitate a fair and qualitative performance analysis and comparison with the InSAR and sea-level results, P036 data were further processed to mitigate the impact of abrupt positioning shifts. Specifically, Segments 2 and 4 remained unchanged due to seemingly good alignment to each other. Segment 1 was systematically shifted in an amount of the vertical mean difference relative to Segment 2. Segments 3 and 5 were shifted in the same way, but the shifts were relative to Segment 4. The further processed P036 time-series are shown as pink circles in Fig. 9. It is noteworthy that residual shifts remain in the processed time-series at P036, particularly between Segments 1 and 2.

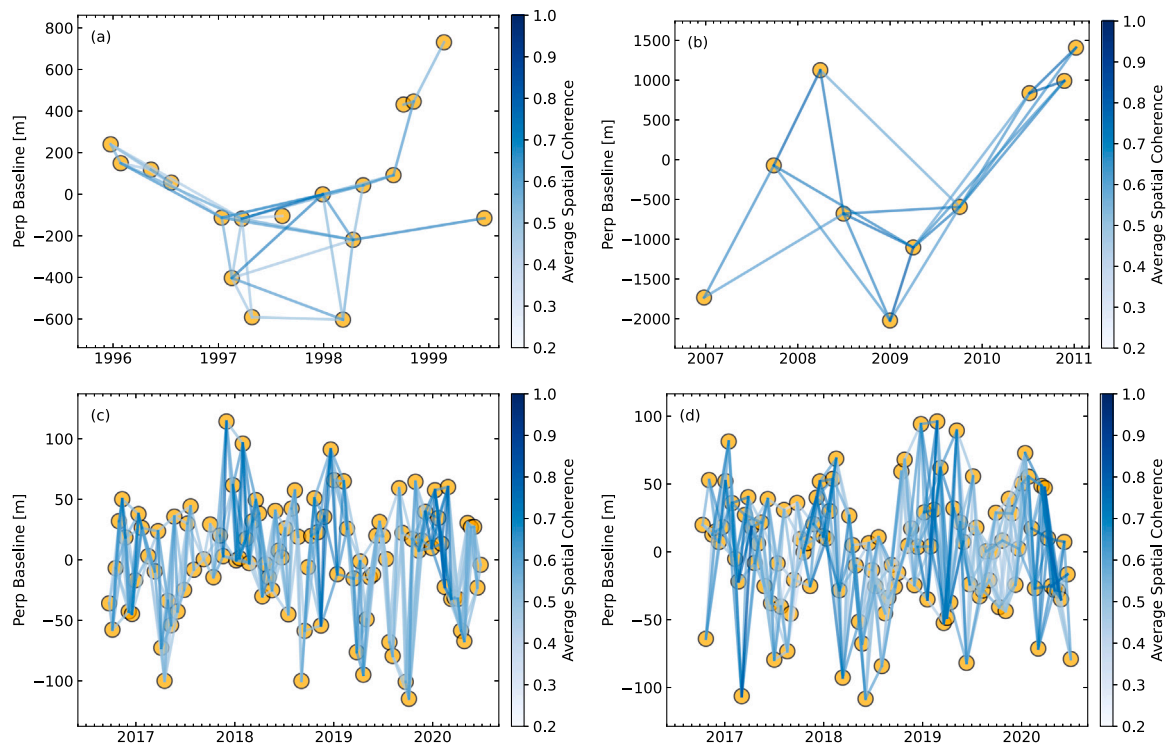


Fig. 3. SBAS network plots between perpendicular and temporal baseline for the SAR data collections of: (a) ERS-2 spanning from 1995 to 1999, (b) ALOS-1 PALSAR spanning from 2007 to 2011, (c) Sentinel-1 ascending orbit spanning from 2016 to 2020, and (d) Sentinel-1 descending orbit spanning from 2016 to 2020. Yellow markers represent the SAR acquisitions, and blue lines are interferogram connections in the network. (For interpretation of the references to color in this figure legend, the reader is referred to the web version of this article.)

4.4. Multi-source VLM estimates at Eagle Point

Time-series results derived from multiple space and terrestrial geodetic techniques including InSAR, GNSS, and sea-level difference between TG and SRA observations were used for VLM performance analysis and comparison near the Eagle Point TG station (i.e., 8771013). Specifically, sea-level difference between the TG and SRA observations was calculated as per Eq. (4) and clear land subsidence patterns after 1998 can be observed from the monthly mean displacement time-series as the blue dots show in Fig. 9 (Qiao et al., 2022). Fig. 9 also includes InSAR results with ERS-2, ALOS-1, and Sentinel-1 land subsidence time-series as well as the vertical positioning results at the P036 cGNSS station as processed in Section 4.3. The Eagle Point TG station is approximately 2.8 km away from the P036 cGNSS station and is less than 400 m apart from the nearest ERS-2, ALOS-1, and Sentinel-1 InSAR grid cells. The independently processed InSAR time-series were manually shifted to align with the sea-level difference results as shown in Fig. 9(a).

Favorable agreement in VLM results can be observed between using InSAR and sea-level difference techniques, and both techniques recovered the subsidence inflection point, in particular, around 1998. The cosine similarity was calculated using $\frac{\mathbf{a} \cdot \mathbf{b}}{\|\mathbf{a}\| \|\mathbf{b}\|}$, where the vector \mathbf{a} is InSAR estimates as shown in Fig. 9(a), the vector \mathbf{b} contains measurements of sea-level difference with the same temporal overlap with InSAR, and the $\|\cdot\|$ operations corresponds to the Euclidean distance of a vector. The cosine value varies between 0 and 1, with higher values indicating greater similarity. In this case study, the cosine similarity value between InSAR and sea-level difference results is approximately 0.96, indicating a strong agreement between the estimates of the two techniques. In addition, overall good agreement in VLM results obtained from P036 cGNSS station and sea-level difference can be observed in Fig. 9(b), although GNSS time-series still exhibit segment offsets after adjustment as processed in Section 4.3. In general, results derived across different geodetic techniques under investigation

demonstrate comparable coastal subsidence performance near the Eagle Point TG station. Meanwhile, coastal subsidence estimated by the monthly mean sea-level difference between TG and SRA observation has the potential of providing longer-term VLM time-series compared with the InSAR or GNSS results due to longer observation history with less observation gaps or disruptions.

4.5. Long-term land subsidence modeling

In order to further examine the ability of monitoring land subsidence patterns with different geodetic techniques near the Eagle Point TG station, two regression models were developed and analyzed. The first model was built by taking both sea-level difference and InSAR results as input data while the second model was trained by using InSAR data alone to investigate the long-term performance without any other geodetic data sources. The Gaussian Process (GP) was adopted for modeling VLM estimates, given it is non-parametric and flexible in fitting non-linear processes, resilient to substantial sample outage, and easy to access confidence interval (Rasmussen and Williams, 2006). The GP is a supervised learning method, where the probability distribution over functions is determined during data fitting with specified covariance function (Rasmussen and Williams, 2006). This indicates that the covariance function (i.e., a kernel function) as well as its parameters need to be learned from the training data despite GP being a non-parametric model that can fit data flexibly (Rasmussen and Williams, 2006). In this study, the radial basis function (RBF) and white Gaussian kernels were used for producing a new kernel as defined in Eq. (5) to fit the VLM estimates:

$$k(x, x') = k_0(x, x') + k_n(x, x') \\ = \left[\theta_1^2 \exp\left(-\frac{(x - x')^2}{2\theta_2^2}\right) \right] + \left[\theta_3^2 \exp\left(-\frac{(x - x')^2}{2\theta_4^2}\right) + \theta_5 \right] \quad (5)$$

where $k_0(x, x')$ is a RBF kernel intended for a smoothing trend and $k_n(x, x')$ is a noise model as the sum of a RBF kernel and an independent

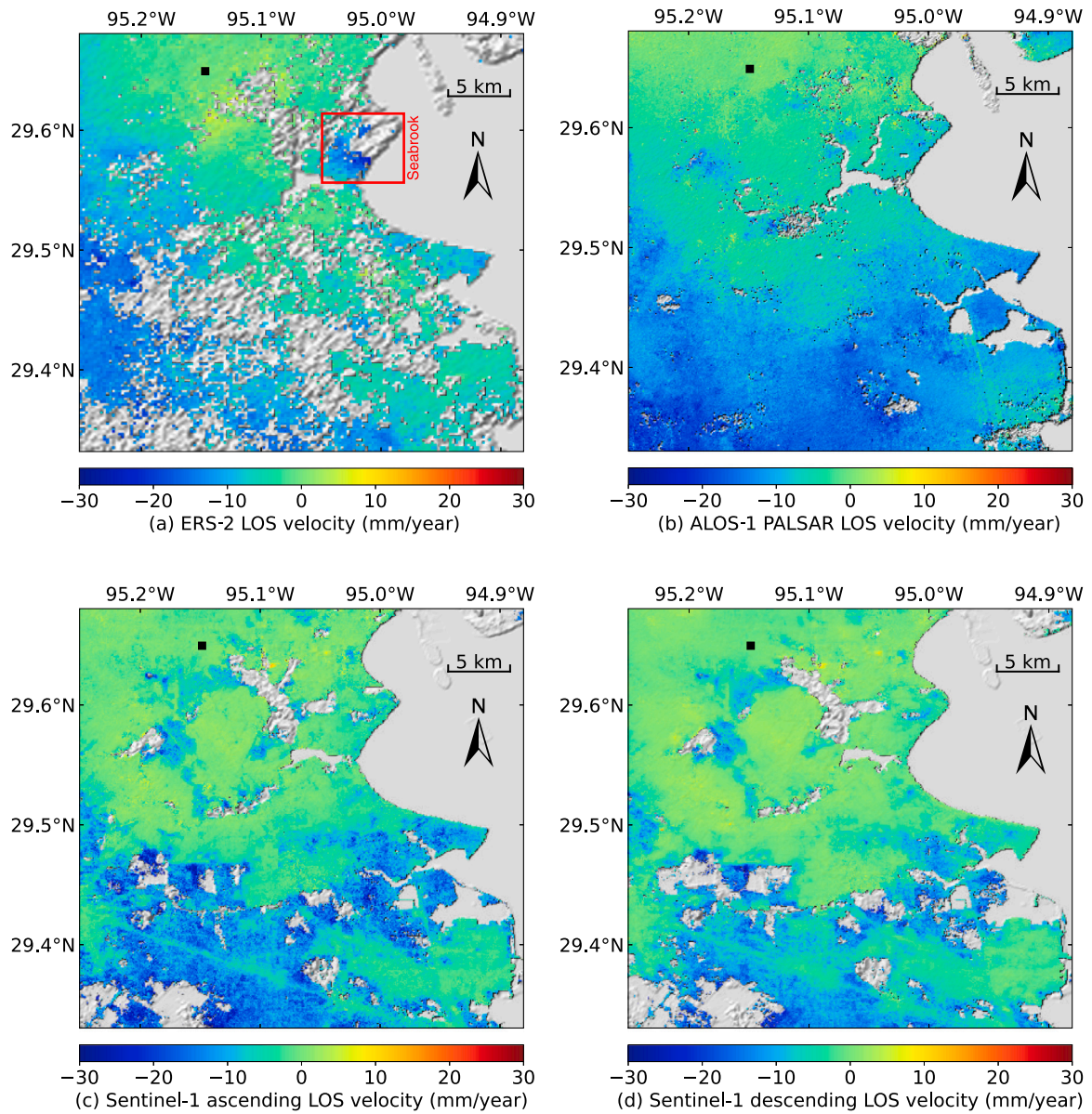


Fig. 4. Land deformation velocity in the LOS direction obtained from acquisitions of: (a) ERS-2 spanning from 1995 to 1999 with the red box highlighting a coastal subsiding hotspot at Seabrook, TX, (b) ALOS-1 PALSAR spanning from 2006 to 2011, (c) Sentinel-1 ascending orbit spanning from 2016 to 2020, and (d) Sentinel-1 descending orbit spanning from 2016 to 2020. The black square in each map corresponds to the reference point, which exhibited high coherence without obvious trend of land deformation. (For interpretation of the references to color in this figure legend, the reader is referred to the web version of this article.)

variance component, x and x' correspond to different time in this work, and $[\theta_1, \theta_2, \dots, \theta_5]$ corresponds to the parameters controlling amplitude (i.e., θ_1, θ_3), characteristic length-scale (i.e., θ_2, θ_4), and noise level (i.e., θ_5 for noise variance) of the GP kernels. Parameters of the kernel were optimized during fitting the Gaussian Process regression (GPR) models.

This study focused on modeling and predicting VLM with the time span between 1993 and 2020. Fig. 10(a) corresponds to VLM processes modeled (i.e., GPR 1) using both InSAR and sea-level difference measurements. Fig. 10(b) illustrates GPR 2 results modeled with InSAR measurements alone. A direct comparison between GPR models 1 and 2 can be found in Fig. 10(c). It can be observed that GPR 1 agreed well with GPR 2 from a long-term perspective, although some offsets can be noticed around 1995, 2002, and 2012 (Fig. 10(d)). Such offsets probably arose from infrequent InSAR measurements, alignment errors of InSAR time-series across different SAR sensors, and so forth. The slope of the difference between GPRs 1 and 2 with a linear regression

was 0.9 mm/yr, which shows the potential of using InSAR technique alone in estimating long-term VLM even if multi-year observation gaps intermittently emerge, particularly at inland areas where other geodetic techniques, such as GNSS, TG, and SRA, are not available. The advantage of using GP models to predict InSAR-based VLM along the coastlines can also be seen from another angle, where long-term RSLC trend can be further estimated by combining both GP-modeled multi-mission InSAR results and SRA observations.

5. Discussion

5.1. Anthropogenic influences on coastal subsidence around Eagle Point

The agreement of VLM results in Section 4.4 may prompt curiosity about the causality associated with observed subsiding processes at Eagle Point. Land subsidence can be classified into two general categories: endogenic subsidence originating within the Earth (e.g., folding,

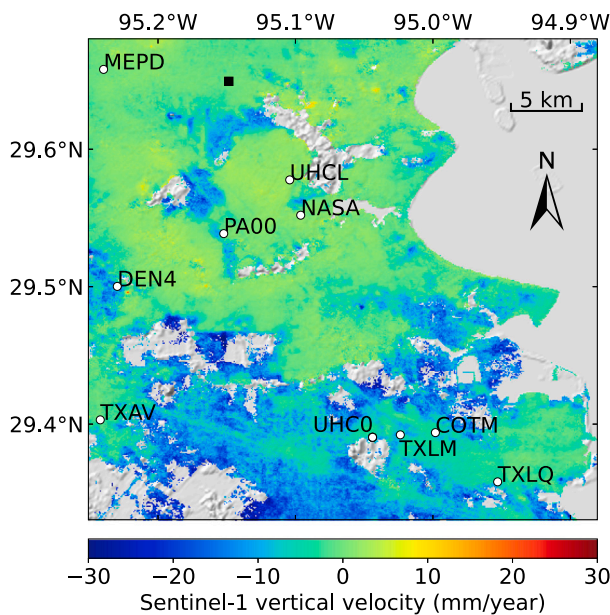


Fig. 5. Vertical velocity map obtained by combining the Sentinel-1 ascending and descending orbit measurements. Circles in the map correspond to cGNSS stations used for validating InSAR results.

faulting, continental drift, etc.) and exogenic subsidence occurring near the earth surface due to both natural and anthropogenic related processes (Prokopovich, 1979). Two main causes of exogenic subsidence are the removal of the solid support, such as mining and karst, and an increasing load on a compressible stratum (e.g., the withdrawal of water and hydrocarbon) (Prokopovich, 1979). Endogenic subsidence tends to bear a regional and sustained trend over time and space and, therefore, the study mainly centered on the exogenic part, which gives rise to varied spatial-temporal patterns of the observed VLM results.

Anthropogenic activities such as fluid (e.g., oil, gas, groundwater) extraction from subsurface reservoirs may cause overlaid rocks to deform. When a reservoir has reached equilibrium before pumping, the geostatic load from its overburden formations is balanced through pore pressure and associated effective stresses (Gambolati et al., 2006). When the fluid head declines after pumping, pressure loss usually distributes more to solid grain-to-grain contacts in the reservoir (i.e., less effective stress contribution from fluid-to-fluid and fluid-to-solid contacts), and the resulting compaction of a drained reservoir may extend to overlaid rocks in the form of land surface subsidence (Gambolati et al., 2006). Although the amount and geographical extent of subsidence caused by hydrocarbon extraction from a local oil/gas trap of a deep-seated and well-consolidated reservoir is usually considered less significant than that caused by groundwater withdrawal from large-scale and shallow aquifer systems (Poland and Davis, 1969; Gambolati et al., 2006), non-negligible amounts of cumulative subsidence have been reported worldwide with reservoir depth over 3048 m (Gambolati et al., 2006; Poland and Davis, 1969; Hermansen et al., 2000; Pratt and Johnson, 1926).

Over the Houston-Galveston region in Texas, groundwater withdrawal was reported to cause rapid land subsidence between the early 1940s and late 1970s due to industrial water use. Moreover, areas far away from Eagle Point are still undergoing land subsidence due to groundwater withdrawal (Greuter et al., 2021). Oil/gas extraction has also contributed to subsidence (Qiao et al., 2023b). For example, an area with a size about $4.0 \times 2.4 \text{ km}^2$ centered at the Goose Creek oil field (approximately 27 km apart from the Eagle Point TG) subsided substantially with a cumulative subsidence of around 1 m between 1918 and 1926 due to oil extraction (Galloway et al., 1999; Pratt and Johnson, 1926).

This study examined anthropogenic activities such as groundwater withdrawal and oil/gas extraction affecting subsidence around Eagle Point, TX. For this study, additional data were utilized to facilitate analysis including: (1) hydrocarbon production from oil/gas wells near the Eagle Point TG station obtained from the RRC of Texas (RRC, 2023) as shown in Fig. 11(a) and (b), (2) monthly Palmer Drought Severity Index (PDSI) time series of the climate division covering Eagle Point (i.e., division 08) (Palmer, 1965; NOAA, 2023b) as demonstrated in Fig. 11(e), and (3) groundwater level measurements of the well KH-64-33-213 from National Water Information System (NWIS) provided by the United States Geological Survey (USGS) (USGS, 2023) as illustrated in Fig. 11(f). It should be noted that there were three oil and gas fields near Eagle Point, including Eagle Bay (Vicksburg), Eagle Bay (Vicksburg 15750), and Eagle Bay (Frio 13200), and the locations of the oil and gas wells from these fields can be found in Fig. 11(h). These fields were mainly composed of gas wells with depths ranging from 4850 to 5457 m. The total gas production (Fig. 11(b)) from all oil and gas wells in the three fields was calculated in billion cubic feet (BCF), including gas volume collected from gas wells and that from casinghead of oil wells. Similarly, Fig. 11(c) reflects the total oil production in million barrels (MMBBL), obtained from oil wells and gas-well condensate. According to RRC, condensate refers to the liquid hydrocarbon recovered by surface separators from natural gas. Only one class II well, which is used to inject fluids associated with hydrocarbon production, was found within the study area (Fig. 11(h)), and its disposal volumes of salt water up to a depth of around 1849 m are shown in Fig. 11(d). Prior investigations revealed that the salt-water disposal caused surface uplift in some localized studies in Texas, and its role in mitigating the subsidence rate in the study area warrants future attention (Shirzaei et al., 2016; Karanam and Lu, 2023). Locations of the Eagle Point TG and the groundwater well, as well as the climate division can be found in Fig. 11(g). The PDSI (Fig. 11(e)) and groundwater level data (Fig. 11(f)) data provided an insight to discover the connection between land subsidence and groundwater usage and withdrawal.

An analysis of Fig. 11 does not suggest that groundwater extraction be responsible for explaining the subsidence around Eagle Point since 1998 because: (1) regulatory action plans have been adopted by HGSD since its foundation in 1975 to reduce groundwater withdrawal (Greuter et al., 2021; Galloway et al., 1999), and (2) a long period of abnormally low rainfall was not for this recorded time period coupled with a rising trend of the groundwater levels (Fig. 11(e) and (f)). Additionally, a temporal coincidence between the inflection of VLM vs. significant increase in oil and gas production can be observed (Fig. 11(a), (b), and (c)). The active oil and gas wells were found located near the Eagle Point TG station (Fig. 11(h)). The solid lines depict casing strings that reach from the reservoir bottoms to the onshore wellheads. Scatter plot of the comparison between land subsidence and cumulative oil/gas extraction around Eagle Point is shown in Fig. 12, where strong negative correlations were discovered. Overall, the findings tend to support that anthropogenic activities related to oil and gas extraction are accountable for land subsidence at Eagle Point.

From a geophysical and geological perspective, the onset and amount of practical land subsidence due to fluid withdrawal depend on geometric and geological settings of related subsurface formations, pumping depth and volume, medium properties (e.g., porosity and compressibility), and so forth (Gambolati et al., 2006). Direct evidence of land subsidence induced by hydrocarbon extraction is the reservoir compaction and the downward movement of overburdened rocks at different depths after pumping. However, finding the direct evidence is not straightforward, and researchers have resorted to examining several crucial conditions occurred to a reservoir, including: (1) a significant drop of pressure, (2) a compressible rock, (3) a considerable thickness, and (4) a small burial depth (Gambolati et al., 2006; Geertsma, 1973). For example, Sharp and Hill showed reservoir depressurization at the Big Hill and Fannett oil fields near the northeastern Texas Gulf Coast using bottom hole pressure (BHP) data, and land subsidence was modeled

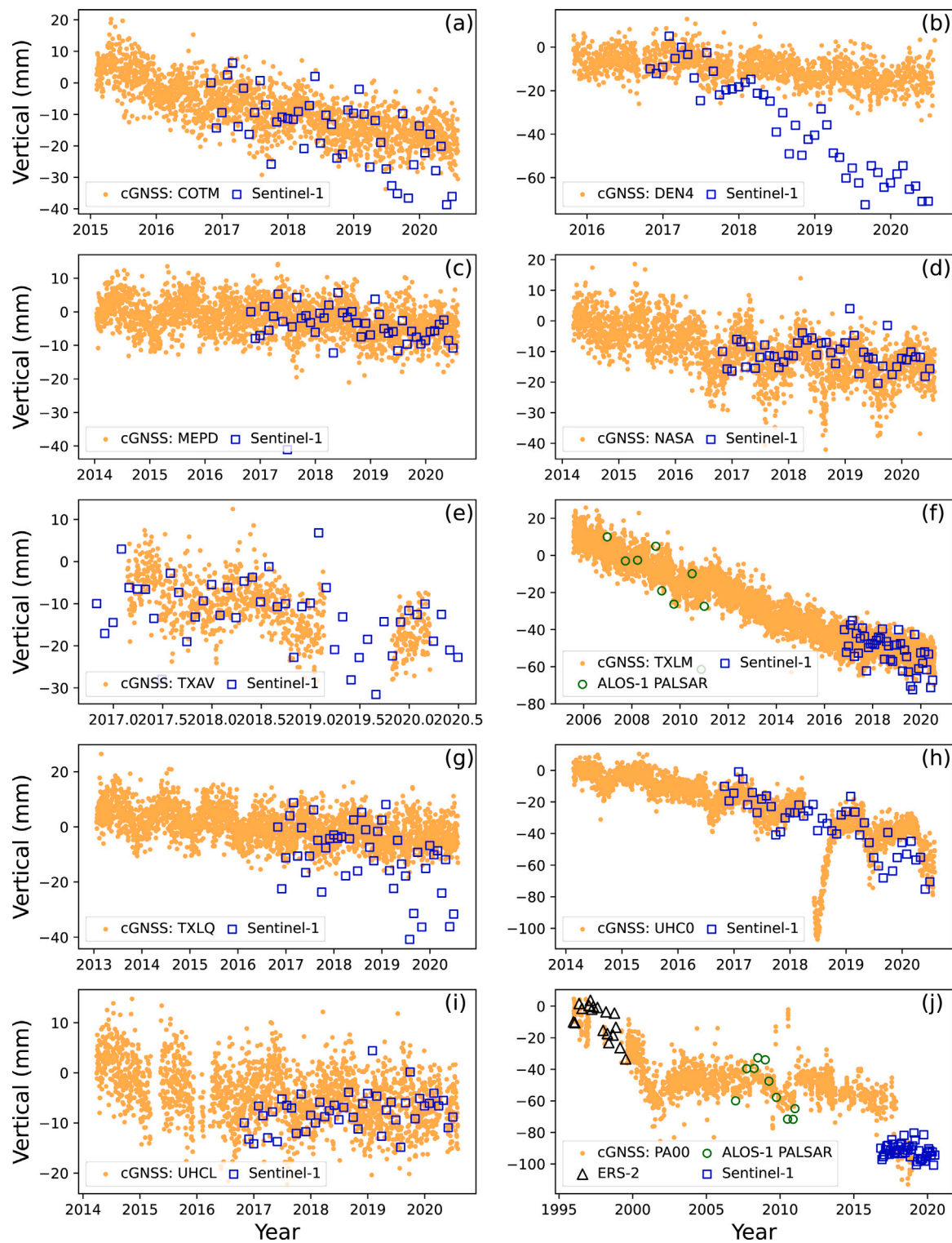


Fig. 6. InSAR time-series validation by comparing with positioning results at ten cGNSS stations in the vertical direction. InSAR time series were vertically shifted for better visualization.

with appropriate hydro-geological parameters (Sharp and Hill, 1995). It is likely that some of these reservoir conditions also hold true in the case of Eagle Point. A surface pressure of approximately 661.9 bar (equivalent to 9600 pounds per square inch (PSI)) at a depth of around 4694 m was reported when a gas well, around 2 km away from San Leon, TX, was being drilled on May 6, 1997, and the Vicksburg interval was reported to be as thick as 610 m (Petzet, 1997). Considering a rapid

rate of fluid extraction after 1998 as shown in Fig. 11(b) and (c), reservoir pressure may have dropped significantly since then. Compared with 1 m cumulative subsidence at Goose Creek oil field with reservoir depths up to 1219 m (Pratt and Johnson, 1926), the observed 0.2 m cumulative land subsidence at Eagle Point is assumed to support the fact that the main Vicksburg formation tends to be more consolidated and less compressible due to deep burial processes. However, further

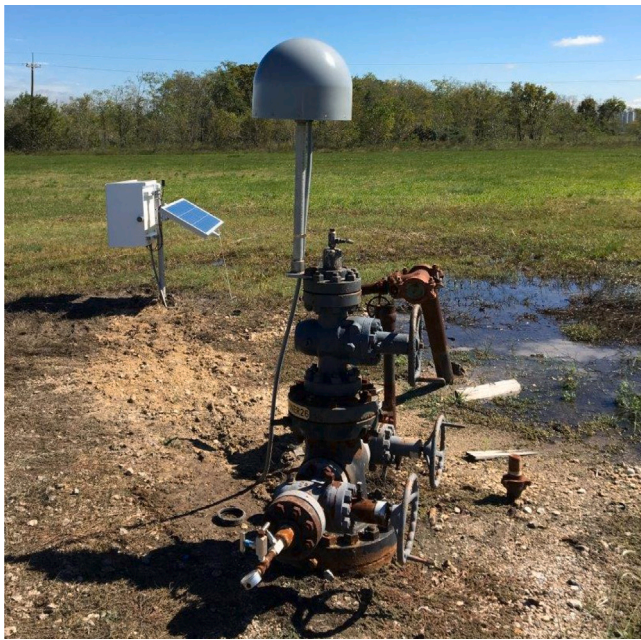


Fig. 7. A photograph of the DEN4 station (UNAVCO, 2023) and its GNSS antenna setup.

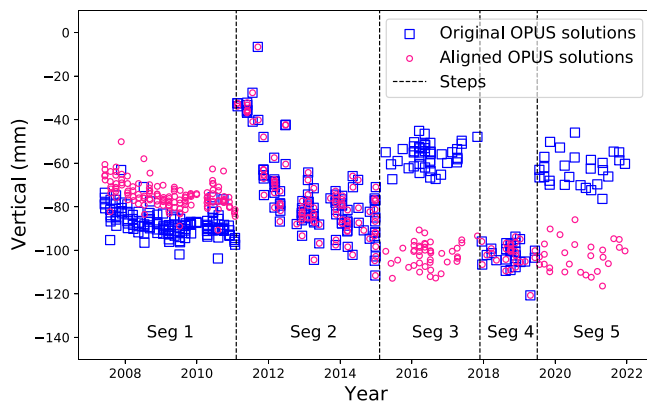


Fig. 8. Positioning time-series in the vertical direction at the P036 cGNSS station. The blue squares represent original P036 solutions. To mitigate the impact of the positioning shifts induced by the frequent antenna changes in the PAM network, Segments 1, 3, and 5 were further processed. Specifically, points in Segment 1 were systematically adjusted in the amount of the vertical mean difference relative to Segment 2. Segments 3 and 5 were shifted in the same way relative to Segment 4.

investigation is needed to explore subsurface activities such as reservoir compaction, fluid dynamics, reservoir geomechanical properties, and so forth (Gambolati et al., 2006).

5.2. Coastal subsidence near Seabrook, TX

Within the study area, another coastal subsidence hotspot is located near Seabrook, TX, as observed between 1995 and 1999 (Fig. 4(a)). The distance between Eagle Point and Seabrook is approximately 14 km. Similar to the analysis near Eagle Point (Fig. 11), hydrocarbon production near Seabrook, TX, and corresponding well locations are shown in Fig. 13. It is evident that hydrocarbon production was mainly extracted before 2000, which explains the presence of VLM in the ERS-2 results rather than in newer SAR acquisitions. Moreover, well locations in Fig. 13 coincide with the geospatial extent in subsidence in Fig. 4(a). The findings suggest that the hydrocarbon withdrawal near

Seabrook, TX, was potentially accountable for land subsidence. Prior studies echoed the conclusions by using the ERS dataset during the 1990s. Specifically, the subsidence near Seabrook, TX, was believed to be driven by hydrocarbon production given the bowl-shape subsidence spatial pattern (i.e., a typical spatial characteristic associated with oil and/or gas extraction) and close proximity to the oil and gas wells (Qu et al., 2015; Buckley et al., 2003).

The well depth near Seabrook, TX, ranged between 2833 and 3890 m, suggesting that the influence of land subsidence associated with oil and gas extraction was not negligible despite the wells being situated at deep-seated reservoirs. This, to some extent, further supports the hypothesis of hydrocarbon-production-induced land subsidence at Eagle Point, given the similar geological settings.

5.3. InSAR estimate

During InSAR data processing, ionospheric corrections were ignored in MintPy, which may have affected the InSAR results through related interferometric phase errors, especially for low-frequency SAR systems (Zhu et al., 2019) such as the ALOS-1 PALSAR employed in this study. In addition, for ERS-2 and ALOS-1 PALSAR, only ascending or descending observations were utilized due to data availability to obtain vertical coastal subsidence by assuming zero land motion in the East–West direction as per Eq. (3). Under such an assumption, vertical displacement estimated from LOS InSAR results may contain errors in case measurable East–West land motion takes place.

When combining InSAR results from multiple platforms, vertical shifts across independently processed time-series segments need to be well determined for a long-term estimate of land subsidence. In this study, the difference in shifting the vertical results between ALOS-1 PALSAR and Sentinel-1 remained the same amount at TXLM cGNSS station (Fig. 6(f)) and at Eagle Point TG (Fig. 9(a)). However, the difference in shifting the vertical results among the same SAR sensors at GNSS PA00 varied. This inconsistency is believed to stem from the discontinuity of PA00 (Fig. 6(j)) mainly due to a series of antenna changes (NGL, 2023). This also implies the challenge of aligning InSAR time series obtained from multiple SAR platforms, especially in cases where long-term continuous GNSS observations tend to be scarce. A larger study area with more reliable cGNSS stations is considered essential for better understanding the amount to which each InSAR time-series results from independent SAR platforms should be aligned.

6. Conclusions

This study combined space and terrestrial geodetic techniques including SBAS InSAR, GNSS, TG, and SRA to investigate coastal subsidence near San Leon, TX, since the 1990s with a focus around the Eagle Point TG station, where sea-level rise relative to the land was reported to be among the highest in the United States. The performance of long-term VLM time-series obtained from multiple SAR platforms (i.e., ERS-2, ALOS-1 PALSAR, and Sentinel-1) were evaluated and validated by comparing with that derived at ten cGNSS stations. VLM processes derived from sea-level difference between TG and SRA observations at the Eagle Point TG station were found consistent with the time-series obtained from InSAR, including the subsidence inflection around 1998, and GNSS results. Anthropogenic activities related to oil and gas extraction are potentially accountable for associated land subsidence around the Eagle Point TG station given the fact that: (1) the TG station and oil/gas wells were in close proximity, (2) land subsidence had shortly started to emerge since the inception of hydrocarbon resource development around 1998, (3) the coastal land kept subsiding as hydrocarbon development continued, and (4) vertical displacements well synchronized with the cumulative hydrocarbon production. In addition, the study modeled VLM processes at Eagle Point with GP using results obtained from sea-level difference and InSAR (i.e., GPR 1) and that from InSAR alone (i.e., GPR 2). Around 0.9 mm/yr trend

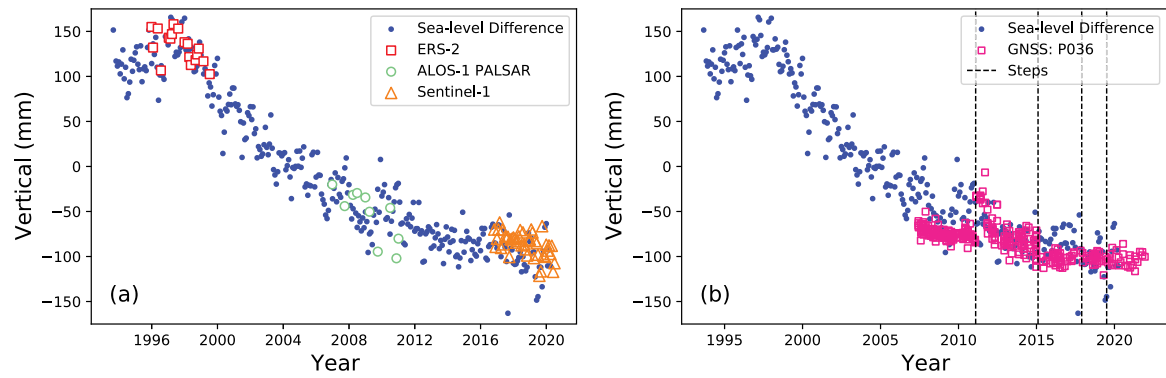


Fig. 9. Land subsidence near the Eagle Point TG station derived from multiple space and terrestrial geodetic techniques: (a) comparison between InSAR vs. monthly mean sea-level difference, and (b) comparison between GNSS vs. monthly mean sea-level difference.

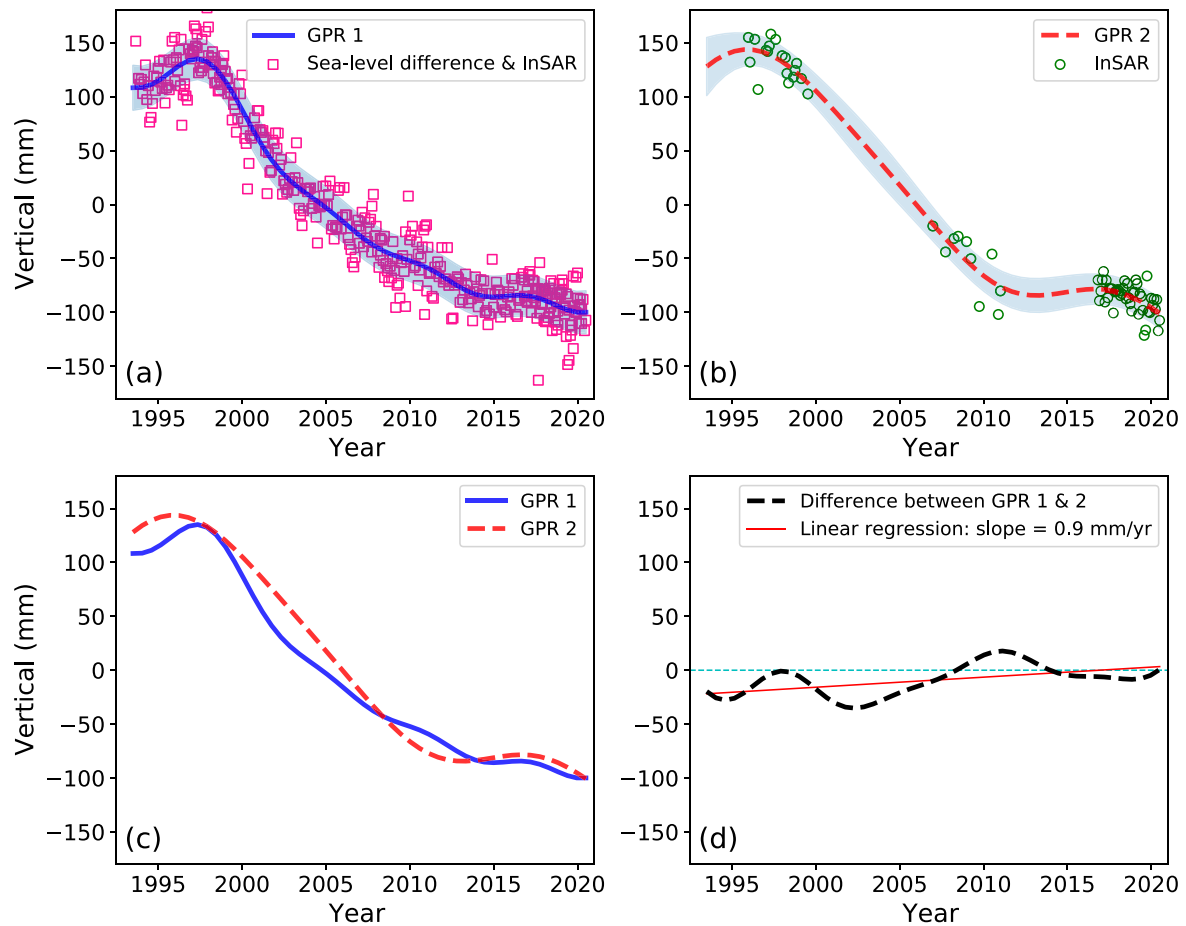


Fig. 10. Time-series modeling of cumulative land subsidence with GP using: (a) both aligned InSAR and sea-level difference results, and (b) InSAR measurements alone. Shaded areas around the regression line in (a) and (b) represent the standard deviation of GP prediction. (c) compares the two GP models, and (d) estimates the offsets between the GP models as well as the corresponding trend. The cyan dashed line in (d) consists of temporal-invariant zero values.

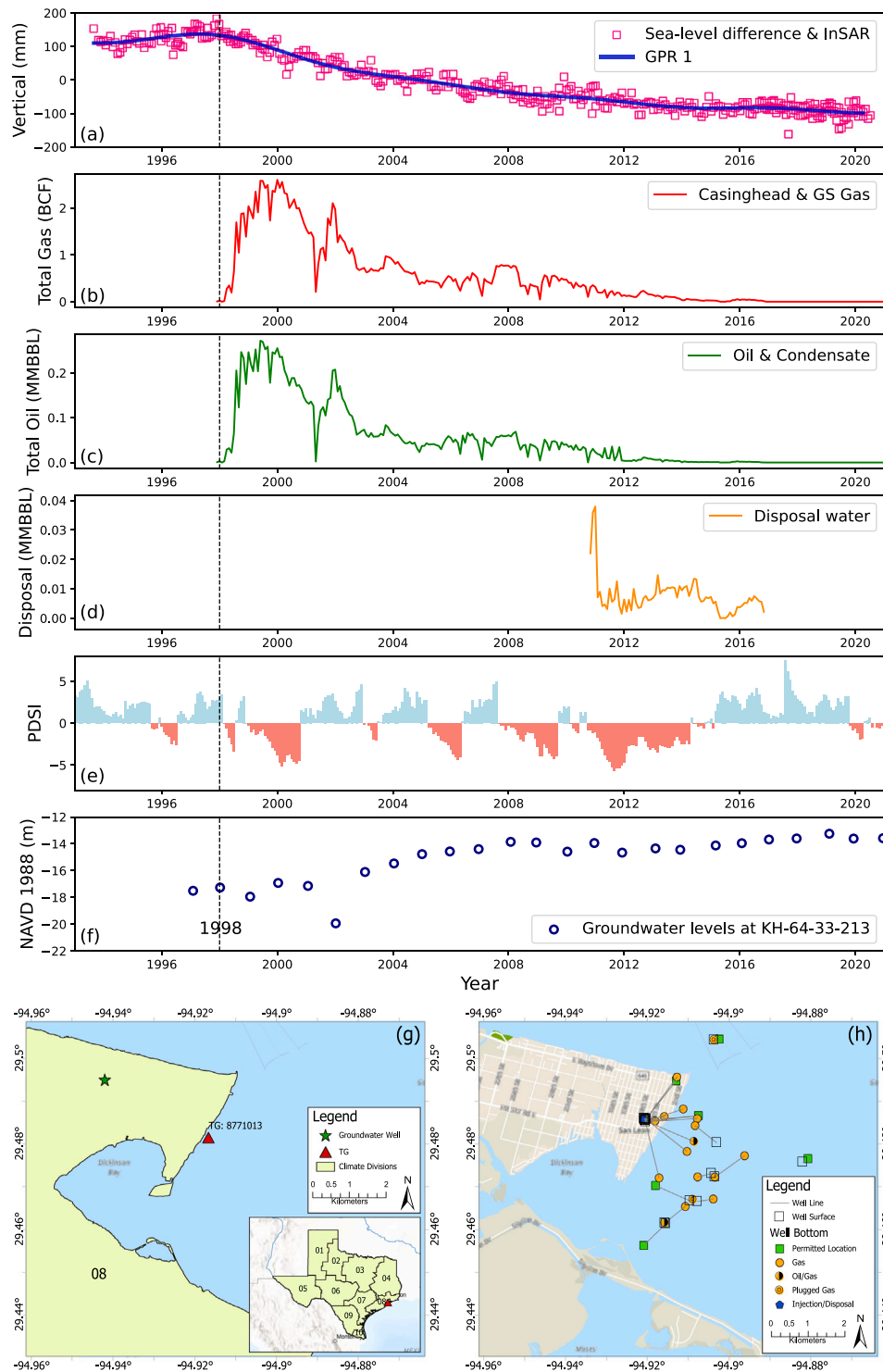


Fig. 11. Cause-and-effect analysis on anthropogenic factors affecting land subsidence around Eagle Point area: (a) cumulative coastal subsidence time-series processed by combining the sea-level difference and InSAR data at the Eagle Point TG station, (b) total gas production from gas wells and oil-well casinghead, (c) total oil production from oil wells and gas-well condensate, (d) water disposal associated with oil/gas activities, (e) PDSI time-series of the “08” climate division zone covering the Eagle Point TG station with negative values in red representing drought and positive in blue for non-drought, (f) groundwater levels at the well KH-64-33-213 at a depth of around 240 m below land surface, (g) a map illustrating the locations of the groundwater well, the Eagle Point TG station, and the coverage of the “08” climate division zone, and (h) a map of oil and gas wells and lines connecting the surface and bottom of the wells. (For interpretation of the references to color in this figure legend, the reader is referred to the web version of this article.)

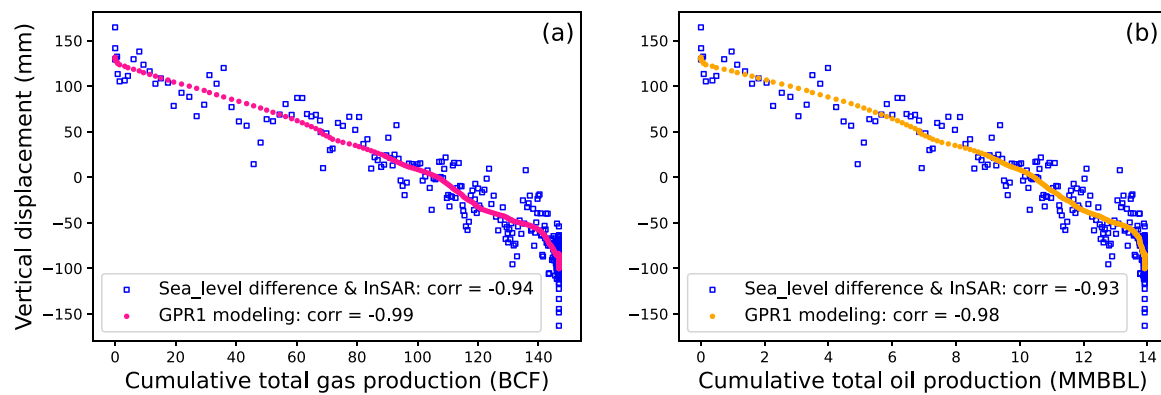


Fig. 12. Scatter plot between vertical displacements (sea-level difference & InSAR as well as their GP modeling) vs. (a) cumulative total gas production and (b) cumulative total oil production. The blue dots display original vertical displacement values combining results obtained from the sea-level difference and InSAR (Fig. 11(a)) after hydrocarbon resource development started around 1998. The pink and orange dots correspond to the displacement values from the GPR 1 regression model as developed in Section 4.5. The correlation coefficient, denoted by *corr*, between vertical displacement and production is provided in the legend. (For interpretation of the references to color in this figure legend, the reader is referred to the web version of this article.)

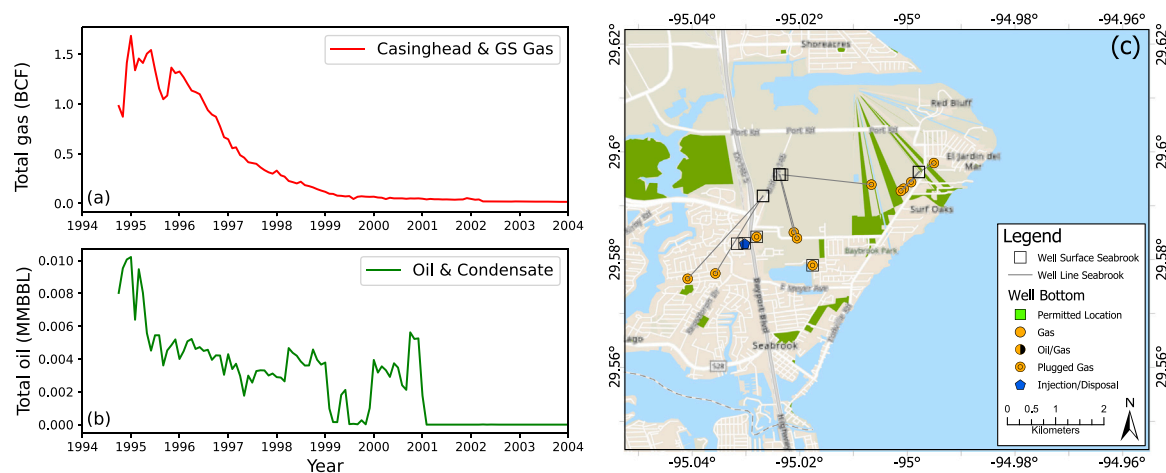


Fig. 13. Hydrocarbon production and corresponding well locations near Seabrook, TX: (a) total gas production from gas wells and oil-well casinghead, (b) total oil production from oil wells and gas-well condensate, and (c) the map of oil and gas locations.

difference was documented between these two GPR models, demonstrating the potential of estimating long-term VLM trend using InSAR results alone even if long observation gaps intermittently occur, particularly at inland areas where the observation data obtained from other geodetic techniques are not available. Future work will concentrate on: (1) including more SAR sensors such as ENVISAT and COSMO-SkyMed to increase data availability and coverage to enhance long-term VLM estimation capabilities, and (2) investigating the potential of RSLC estimation along coastal Texas by employing multiple space geodetic techniques and validating its performance through comparing with the measurements obtained from TG stations.

CRedit authorship contribution statement

XiaoJun Qiao: Conceptualization, Methodology, Data curation, Validation, Formal analysis, Investigation, Writing – original draft, Writing – review & editing. **Tianxing Chu:** Formal analysis, Writing – original draft. **Philippe Tissot:** Resources, Writing – review & editing. **Seneca Holland:** Writing – review & editing.

Declaration of competing interest

The authors declare that they have no known competing financial interests or personal relationships that could have appeared to influence the work reported in this paper.

Data availability

Data will be made available on request.

Acknowledgments

This research was supported by the U.S. Department of Commerce-National Oceanic and Atmospheric Administration (NOAA) through the University of Southern Mississippi (USM) under the terms of Agreement [No. NA13NOS4000166]. This work was also supported by the National Science Foundation (NSF) under award No. 2131263. The authors also thank the Open Access Publication Fund provided by the Mary and Jeff Bell Library at Texas A&M University-Corpus Christi (TAMU-CC). Opinions expressed by authors herein do not necessarily reflect views of NOAA, NSF or USM. The authors are grateful to Dr. Laha Ale for his valuable review and insightful comments on the article.

Appendix A. Supplementary data

The supplementary file contains formation information of the study area (Table S1 and S2), date information for ERS-2, ALOS-1 PALSAR, and Sentinel-1 SAR images used in this study (i.e., from Table S3 to S6), detailed description of cGNSS stations (Table S7), and description for TG stations (Table S8).

References

- ASF, 2022. ASF data search vertex. URL <https://asf.alaska.edu/>, Copernicus Sentinel data. Retrieved from ASF DAAC [07/01/2022 of data access], processed by ESA..
- Berardino, P., Fornaro, G., Lanari, R., Sansosti, E., 2002. A new algorithm for surface deformation monitoring based on small baseline differential SAR interferograms. *IEEE Trans. Geosci. Remote Sens.* 40 (11), 2375–2383.
- Bertiger, W., Bar-Sever, Y., Dorsey, A., Haines, B., Harvey, N., Hemberger, D., Hefflin, M., Lu, W., Miller, M., Moore, A.W., et al., 2020. GipsyX/RTGx, a new tool set for space geodetic operations and research. *Adv. Space Res.* 66 (3), 469–489.
- Blewitt, G., Hammond, W.C., Kreemer, C., 2018. Harnessing the GPS data explosion for interdisciplinary science. *Eos* 99 (10.1029), 485.
- Buckley, S.M., Rosen, P.A., Hensley, S., Tapley, B.D., 2003. Land subsidence in Houston, Texas, measured by radar interferometry and constrained by extensometers. *J. Geophys. Res.: Solid Earth* 108 (B11).
- Castellazzi, P., Garfias, J., Martel, R., 2021. Assessing the efficiency of mitigation measures to reduce groundwater depletion and related land subsidence in Querétaro (Central Mexico) from decadal InSAR observations. *Int. J. Appl. Earth Obs. Geoinf.* 105, 102632.
- Cazenave, A., Dominh, K., Ponchaut, F., Soudarin, L., Cretaux, J., Le Provost, C., 1999. Sea level changes from Topex-Poseidon altimetry and tide gauges, and vertical crustal motions from DORIS. *Geophys. Res. Lett.* 26 (14), 2077–2080.
- Chen, B., Gong, H., Chen, Y., Lei, K., Zhou, C., Si, Y., Li, X., Pan, Y., Gao, M., 2021. Investigating land subsidence and its causes along Beijing high-speed railway using multi-platform InSAR and a maximum entropy model. *Int. J. Appl. Earth Obs. Geoinf.* 96, 102284.
- Chen, C.W., Zebker, H.A., 2002. Phase unwrapping for large SAR interferograms: Statistical segmentation and generalized network models. *IEEE Trans. Geosci. Remote Sens.* 40 (8), 1709–1719.
- Chen, X., Zhang, X., Church, J.A., Watson, C.S., King, M.A., Monselesan, D., Legresy, B., Harig, C., 2017. The increasing rate of global mean sea-level rise during 1993–2014. *Nat. Clim. Chang.* 7 (7), 492–495.
- Combes, J.M., 1993. The Vicksburg Formation of Texas: Depositional systems distribution, sequence stratigraphy, and petroleum geology. *AAPG Bull.* 77 (11), 1942–1970.
- Costantini, M., 1998. A novel phase unwrapping method based on network programming. *IEEE Trans. Geosci. Remote Sens.* 36 (3), 813–821.
- Crocetti, L., Scharfner, M., Soja, B., 2021. Discontinuity detection in GNSS station coordinate time series using machine learning. *Remote Sens.* 13 (19), <http://dx.doi.org/10.3390/rs13193906>, URL <https://www.mdpi.com/2072-4292/13/19/3906>.
- DEOS, 2022. ERS precise orbit determination by the delft institute for earth-oriented space research (DEOS). URL <http://www.deos.tudelft.nl/ers/precors/orbits/>. (Accessed 20 December 2022).
- Earth Resources Observation and Science (EROS) Center, 2017. Shuttle radar topography mission (SRTM) 1 arc-second global.
- El Shouny, A., Miky, Y., 2019. Accuracy assessment of relative and precise point positioning online GPS processing services. *J. Appl. Geod.* 13 (3), 215–227.
- Epps, J.C., Khan, S.D., 2016. Subsidence and sea level rise measurements for Houston and Galveston, Texas. In: 2016 IEEE International Geoscience and Remote Sensing Symposium. IGARSS. IEEE, pp. 7698–7700.
- E.U. Copernicus Marine Service Information, 2022. Global ocean gridded 14 sea surface heights and derived variables reprocessed (1993–ongoing). <http://dx.doi.org/10.48670/moi-00148>.
- Fialko, Y., Simons, M., Agnew, D., 2001. The complete (3-D) surface displacement field in the epicentral area of the 1999 Mw7. 1 Hector Mine earthquake, California, from space geodetic observations. *Geophys. Res. Lett.* 28 (16), 3063–3066.
- Galloway, W.E., Hobday, D.K., Magara, K., 1982. Frio Formation of the Texas Gulf Coast Basin: depositional systems, structural framework, and hydrocarbon, origin, migration, distribution, and exploration potential. Report of investigations No. 122. Technical Report, Texas Univ., Austin (USA). Bureau of Economic Geology.
- Galloway, D.L., Jones, D.R., Ingebritsen, S.E., 1999. Land Subsidence in the United States. Vol. 1182, US Geological Survey.
- Gambolati, G., Teatini, P., Ferronato, M., 2006. Anthropogenic land subsidence. *Encycl. Hydrol. Sci.*
- Geertsma, J., 1973. Land subsidence above compacting oil and gas reservoirs. *J. Pet. Tech.* 25 (06), 734–744.
- Gregory, J.L., 1966. A lower oligocene delta in the subsurface of southeastern Texas. *Gulf Coast Assoc. Geol. Soc. Trans.* 16, 227–241.
- Greuter, A., Turco, M., Petersen, C., Wang, G., 2021. Impacts of groundwater withdrawal regulation on subsidence in Harris and Galveston counties, Texas, 1978–2020. *GeoGulf Trans.* 71, 109–118.
- Hanssen, R.F., 2001. Radar Interferometry: Data Interpretation and Error Analysis. Vol. 2, Springer Science & Business Media.
- Hermansen, H., Landa, G., Sylte, J., Thomas, L., 2000. Experiences after 10 years of waterflooding the Ekofisk Field, Norway. *J. Pet. Sci. Eng.* 26 (1–4), 11–18.
- Hersbach, H., Dee, D., 2016. ERA5 reanalysis is in production. *ECMWF Newsl.* 147 (7), 5–6.
- Hexagon, 2023. HxGN SmartNet. URL <https://www.smartnetna.com/portal/>.
- Hirsch, M., 2018. PyMap3D: 3-D coordinate conversions for terrestrial and geospace environments. *J. Open Source Softw.* 3 (23), 580.
- Hogenson, K., Arko, S.A., Buechler, B., Hogenson, R., Herrmann, J., Geiger, A., 2016. Hybrid pluggable processing pipeline (HyP3): A cloud-based infrastructure for generic processing of SAR data. In: AGU Fall Meeting Abstracts. Vol. 2016, pp. IN21B–1740.
- Holzer, T.L., Johnson, A.I., 1985. Land subsidence caused by ground water withdrawal in urban areas. *Geoj.* 11 (3), 245–255.
- Hooper, A., Zebker, H., Segall, P., Kampes, B., 2004. A new method for measuring deformation on volcanoes and other natural terrains using InSAR persistent scatterers. *Geophys. Res. Lett.* 31 (23).
- Hyne, N.J., 1984. Geology for Petroleum Exploration, Drilling and Production. Pennwell Books, Tulsa, OK.
- Jolivet, R., Grandin, R., Lasserre, C., Doin, M.-P., Peltzer, G., 2011. Systematic InSAR tropospheric phase delay corrections from global meteorological reanalysis data. *Geophys. Res. Lett.* 38 (17).
- Karanam, V., Lu, Z., 2023. Hydrocarbon production induced land deformation over Permian Basin; analysis using persistent scatterer interferometry and numerical modeling. *Int. J. Appl. Earth Obs. Geoinf.* 122, 103424.
- Kuo, C., Shum, C., Braun, A., Mitrovica, J., 2004. Vertical crustal motion determined by satellite altimetry and tide gauge data in Fennoscandia. *Geophys. Res. Lett.* 31 (1).
- LEGOS/CNRS/CLS, 1992. Dynamic atmospheric correction. <http://dx.doi.org/10.24400/527896/A01-2022.001>, URL <https://www.aviso.altimetry.fr/en/data/products/auxiliary-products/dynamic-atmospheric-correction.html>.
- Letetrel, C., Karpytchev, M., Bouin, M.-N., Marcos, M., Santamaría-Gómez, Á., Wöppelmann, G., 2015. Estimation of vertical land movement rates along the coasts of the Gulf of Mexico over the past decades. *Cont. Shelf Res.* 111, 42–51.
- McGranahan, G., Balk, D., Anderson, B., 2007. The rising tide: assessing the risks of climate change and human settlements in low elevation coastal zones. *Environ. Urban.* 19 (1), 17–37.
- Motagh, M., Shamshiri, R., Haghighi, M.H., Wetzel, H.-U., Akbari, B., Nahavandchi, H., Roessner, S., Arabi, S., 2017. Quantifying groundwater exploitation induced subsidence in the Rafsanjan plain, southeastern Iran, using InSAR time-series and in situ measurements. *Eng. Geol.* 218, 134–151.
- National Research Council, 1991. Mitigating Losses from Land Subsidence in the United States. The National Academies Press, Washington, DC, <http://dx.doi.org/10.17226/1796>, URL <https://nap.nationalacademies.org/catalog/1796/mitigating-losses-from-land-subsidence-in-the-united-states>.
- NGL, 2023. Precise point positioning (PPP) product of GNSS observations by Nevada Geodetic Lab (NGL). URL <http://geodesy.unr.edu/>. (Accessed 12 March 2023).
- NOAA, 2023a. 8771013 Eagle Point, Galveston Bay, TX. URL <https://tidesandcurrents.noaa.gov/ports/ports.html?id=8771013&mode=allct>. (Accessed 1 January 2023).
- NOAA, 2023b. National centers for environmental information (NCEI): the palmer drought severity index. Online <https://www.nci.noaa.gov/pub/data/cirs/climdiv/climdiv-pdsidv-v1.0.0-20230707>. (Accessed 1 March 2023).
- NOAA, 2023c. OPUS: the online positioning user service. URL <https://www.ngs.noaa.gov/OPUS/>.
- Palmer, W.C., 1965. Meteorological Drought. Vol. 30, US Department of Commerce, Weather Bureau.
- Petzet, G.A., 1997. Vicksburg, Frio successes lift Galveston Bay area prospects. *Oil Gas J.* 95 (32).
- Poland, J.F., Davis, G.H., 1969. Land subsidence due to withdrawal of fluids. *Rev. Eng. Geol.*
- Pratt, W.E., Johnson, D.W., 1926. Local subsidence of the Goose Creek oil field. *J. Geol.* 34 (7, Part 1), 577–590.
- Prokopovich, N.P., 1979. Genetic classification of land subsidence. In: Evaluation and Prediction of Subsidence. ASCE, pp. 389–399.
- Qiao, X., Chu, T., Tissot, P., Ali, I., Ahmed, M., 2023a. Vertical land motion monitored with satellite radar altimetry and tide gauge along the Texas coastline, USA, between 1993 and 2020. *Int. J. Appl. Earth. Obs. Geoinf.* 117, 103222.
- Qiao, X., Chu, T., Tissot, P., Holland, S., 2023b. Sentinel-1 InSAR-derived land subsidence assessment along the Texas Gulf Coast. *Int. J. Appl. Earth. Obs. Geoinf.* 125, 103544.
- Qiao, X., Chu, T., Tissot, P., Louis, J., 2021. Land subsidence with tide gauge, radar altimetry and GNSS: A case study at Subsiding Coast in Texas. In: 34th International Technical Meeting of the Satellite Division of the Institute of Navigation. ION GNSS+ 2021. pp. 3956–3962.
- Qiao, X., Chu, T., Tissot, P., Louis, J., Ali, I., 2022. Land subsidence estimation with tide gauge and satellite radar altimetry measurements along the Texas Gulf Coast, USA. *IEEE Geosci. Remote Sens. Lett.* 19, 1–5.
- Qu, F., Lu, Z., Zhang, Q., Bawden, G.W., Kim, J.-W., Zhao, C., Qu, W., 2015. Mapping ground deformation over Houston–Galveston, Texas using multi-temporal InSAR. *Remote Sens. Environ.* 169, 290–306.
- Rasmussen, C.E., Williams, C.K.I., 2006. Gaussian Processes for Machine Learning. The MIT Press, <http://dx.doi.org/10.7551/mitpress/3206.001.0001>.
- Rosen, P.A., Gurrola, E., Sacco, G.F., Zebker, H., 2012. The InSAR scientific computing environment. In: EUSAR 2012; 9th European Conference on Synthetic Aperture Radar. VDE, pp. 730–733.
- RRC, 2023. The railroad commission of Texas. <https://www.rrc.texas.gov/>. (Accessed 1 January 2023).

- Santamaría-Gómez, A., Gravelle, M., Wöppelmann, G., 2014. Long-term vertical land motion from double-differenced tide gauge and satellite altimetry data. *J. Geod.* 88 (3), 207–222.
- Scharroo, R., Visser, P., 1998. Precise orbit determination and gravity field improvement for the ERS satellites. *J. Geophys. Res. Oceans* 103 (C4), 8113–8127.
- Sharp, J., Hill, D., 1995. Land subsidence along the northeastern Texas Gulf coast: Effects of deep hydrocarbon production. *Environ. Geol.* 25, 181–191.
- Shirzaei, M., Ellsworth, W.L., Tiampo, K.F., González, P.J., Manga, M., 2016. Surface uplift and time-dependent seismic hazard due to fluid injection in eastern Texas. *Sci.* 353 (6306), 1416–1419.
- Shirzaei, M., Freymueller, J., Törnqvist, T.E., Galloway, D.L., Dura, T., Minderhoud, P.S., 2021. Measuring, modelling and projecting coastal land subsidence. *Nat. Rev. Earth Environ.* 2 (1), 40–58.
- Simons, M., Rosen, P., 2007. Interferometric synthetic aperture radar geodesy. *Geod.* 3, 391–446.
- Soler, T., Weston, N.D., Foote, R.H., 2011. CORS and OPUS for Engineers: Tools for Surveying and Mapping Applications. ASCE Publications, p. 17.
- Sweet, W., Simon, S., Dusek, G., Marcy, D., Brooks, W., Pendleton, M., Marra, J., 2021. 2021 State of high tide flooding and annual outlook. NOAA Technical Reports, pp. 1–20.
- Tang, W., Zhan, W., Jin, B., Motagh, M., Xu, Y., 2021. Spatial variability of relative sea-level rise in Tianjin, China: Insight from InSAR, GPS, and tide-gauge observations. *IEEE J. Sel. Top. Appl. Earth Obs. Remote Sens.* 14, 2621–2633.
- Tay, C., Lindsey, E.O., Chin, S.T., McCaughey, J.W., Bekaert, D., Nguyen, M., Hua, H., Manipon, G., Karim, M., Horton, B.P., et al., 2022. Sea-level rise from land subsidence in major coastal cities. *Nat. Sustain.* 1–9.
- UNAVCO, 2022. Seamless SAR archive (SSARA) data search and access. URL <https://web-services.unavco.org/brokered/ssara/gui>. (Accessed 20 December 2022).
- UNAVCO, 2023. GNSS monitoring networks. URL <https://www.unavco.org/instrumentation/networks/status/notes/photos/DEN4>. (Accessed 1 January 2023).
- USGS, 2023. National water information system of United States geological survey (USGS). Online <https://nwis.waterdata.usgs.gov/nwis/gwlevels>. (Accessed 1 July 2023).
- Wang, G., Li, P., Li, Z., Liang, C., Wang, H., 2022. Coastal subsidence detection and characterization caused by brine mining over the Yellow River Delta using time series InSAR and PCA. *Int. J. Appl. Earth Obs. Geoinf.* 114, 103077.
- Wang, G., Soler, T., 2013. Using OPUS for measuring vertical displacements in Houston, Texas. *J. Surv. Eng.* 139 (3), 126–134.
- Wang, G., Soler, T., 2015. Measuring land subsidence using GPS: Ellipsoid height versus orthometric height. *J. Surv. Eng.* 141 (2), 05014004.
- Woodworth, P.L., Melet, A., Marcos, M., Ray, R.D., Wöppelmann, G., Sasaki, Y.N., Cirano, M., Hibbert, A., Huthnance, J.M., Monserrat, S., et al., 2019. Forcing factors affecting sea level changes at the coast. *Surv. Geophys.* 40 (6), 1351–1397.
- Wöppelmann, G., Marcos, M., 2016. Vertical land motion as a key to understanding sea level change and variability. *Rev. Geophys.* 54 (1), 64–92.
- Wöppelmann, G., Miguez, B.M., Bouin, M.-N., Altamimi, Z., 2007. Geocentric sea-level trend estimates from GPS analyses at relevant tide gauges world-wide. *Glob. Planet. Change* 57 (3–4), 396–406.
- Wright, T.J., Parsons, B.E., Lu, Z., 2004. Toward mapping surface deformation in three dimensions using insar. *Geophys. Res. Lett.* 31 (1).
- Yu, J., Wang, G., 2017. Introduction to the GNSS geodetic infrastructure in the Gulf of Mexico Region. *Surv. Rev.* 49 (352), 51–65.
- Yunjun, Z., Fattahi, H., Amelung, F., 2019. Small baseline InSAR time series analysis: Unwrapping error correction and noise reduction. *Comput. Geosci.* 133, 104331.
- Zhong, W., Chu, T., Tissot, P., Wu, Z., Chen, J., Zhang, H., 2022. Integrated coastal subsidence analysis using InSAR, LiDAR, and land cover data. *Remote Sens. Environ.* 282, 113297.
- Zhu, W., Jung, H.-S., Chen, J.-Y., 2019. Synthetic aperture radar interferometry (InSAR) ionospheric correction based on faraday rotation: two case studies. *Appl. Sci.* 9 (18), 3871.
- Zilkoski, D.B., Hall, L.W., Mitchell, G.J., Kammula, V., Singh, A., Chrismer, W.M., Neighbors, R.J., 2003. The harris-galveston coastal subsidence district/national geodetic survey automated global positioning system subsidence monitoring project. In: *Proceedings of the US Geological Survey Subsidence Interest Group Conference*. US Geological Survey, pp. 13–28.